Supplementary Information

Control of site-specific deprotonation through mechanochemical interconversion of two ionic cocrystal forms of resveratrol

Bowyn D. Ziebarth,[a] Liulei Ma,[a] Gary C. George III,[a] and Kristin M. Hutchins[a,b]*

[a]Department of Chemistry, University of Missouri, 601 S College Avenue, Columbia, Missouri, 65211, United States of America.

[b]MU Materials Science & Engineering Institute, University of Missouri, Columbia, Missouri, 65211, United States of America.

*Email: kristin.hutchins@missouri.edu

1. Experimental Details

Materials

Resveratrol (RSV) was purchased from Oakwood Chemical (Columbia, SC, USA). 4-Aminopyridine (4AP) was purchased from Acros Organics (Fair Lawn, NJ, USA). Ethyl acetate and hexanes were purchased from Fisher Scientific (Fair Lawn, NJ, USA).

Slurry experiments

The 1:1 phase (phase **1**) was initially produced via slurry method by adding RSV and 4AP in a 1:1 molar ratio to a small amount of ethyl acetate or chloroform and stirring overnight. The resulting product was filtered and analyzed via PXRD.

The 1:2 hydrate phase (phase **2**) was initially produced via slurry method by adding RSV and 4AP in a 1:3 molar ratio to a small amount of chloroform and stirring overnight. The resulting product was filtered and analyzed via PXRD.

Liquid-assisted grinding (LAG) experiments

Grinding experiments were performed using a FlackTek SpeedMixer 300-100 SE purchased from FlackTek manufacturing. Stainless steel milling jars and milling balls were acquired from Form-Tech Scientific. Prior to milling, the jars were placed in a custom holder acquired from FlackTek.

Phase **1** was prepared by placing equimolar amounts of RSV (70.8 mg, 0.31 mmol) and 4AP (29.2 mg, 0.31 mmol) along with 30 µL ethyl acetate and one 10 mm stainless steel grinding ball in a 15 mL stainless steel milling jar. The mixture was then milled at 1500 rpm for 10 minutes. The product was allowed to air dry for a few hours, then powder X-ray diffraction (PXRD) was performed.

Phase **2** was prepared by placing 44.8 mg RSV (0.2 mmol), 55.3 mg 4AP (0.6 mmol), 30 µL H_2O, and one 10 mm stainless steel grinding ball in a 15 mL stainless steel milling jar. The mixture was then milled at 1500 rpm for 10 minutes. The product was allowed to air dry for a few hours, then PXRD was performed.

Phase **2** was also prepared by milling RSV and 4AP in a 1:2.5 or 1:2 molar ratio.

Interconversion milling experiments

Interconversion experiments were performed in 15 mL stainless steel milling jars with one 10 mm stainless steel grinding ball.

First, phase **1** was produced by placing 70.8 mg (0.31 mmol) RSV, 29.2 mg (0.31 mmol) 4AP, and 30 µL ethyl acetate in a milling jar, which was then milled at 1500 rpm for 10 minutes. PXRD confirmed formation of phase **1**.

To convert phase **1** into phase **2**, 100 mg of phase **1** was placed in a milling jar, followed by addition of 58.4 mg (0.62 mmol) 4AP and 30 µL H_2O. The components were then milled at 1500 rpm for 10 minutes, which afforded phase **2** as evidenced by PXRD.

To convert phase **2** to phase **1**, 100 mg of phase **2** was placed in a milling jar, followed by 89.4 mg (0.39 mmol) RSV and 30 µL ethyl acetate. The components were then milled at 1500 rpm for 10 minutes, which yielded phase **1** based on PXRD.

These conversions were able to be repeated twice, in sequence, to afford the appropriate phases, i.e., phase **1** was produced, then converted into phase **2**, then converted back into phase **1**, then converted into phase **2** a second time, then converted back into phase **1**.

Notably, heating phase **2** in either ambient or inert atmosphere degrades the product, rather than converting to phase **1**.

The role of stoichiometry and solvent was also elucidated to determine a mechanism of interconversion between phase **1** and phase **2**.

To determine if stoichiometry is the primary condition for conversion, 100 mg of phase **1** was placed in a milling jar, followed by addition of 58.4 mg 4AP. The components were then milled at 1500 rpm for 10 minutes and analyzed via PXRD.

Similarly, 100 mg of phase **2** was placed in a milling jar, followed by addition of 89.4 mg RSV. The components were then milled at 1500 rpm for 10 minutes and analyzed via PXRD.

To determine if solvent is the primary condition for conversion, 100 mg of phase **1** was placed in a milling jar, followed by 30 µL H_2O. The components were then milled at 1500 rpm for 10 minutes and analyzed via PXRD.

Similarly, 100 mg of phase **2** was placed in a milling jar, followed by addition of 30 µL EtOAc. The components were then milled at 1500 rpm for 10 minutes and analyzed via PXRD.

Crystallization

When crystallizing either phase, methanol, ethanol, and water were not used, as deprotonated RSV reacts with these solvents, degrading in solution.

Phase 1: Crystals of phase **1** were grown by dissolving 60.5 mg RSV (0.27 mmol) and 25.0 mg 4AP (0.27 mmol) in 3 mL ethyl acetate. Slow evaporation of the solution yielded crystals suitable for X-ray diffraction.

Crystals of phase **1** were also grown by dissolving approximately 10 mg of interconversion products with a 1:1 mole ratio in 2 mL ethyl acetate in a small vial, then vapor diffusing against hexanes. After several days of vapor diffusion, crystals suitable for X-ray diffraction grew on the inside wall of the vial.

Phase 2: Crystals of phase **2** were grown by dissolving approximately 5 mg of the product from milling (1:3 ratio RSV:4AP) in 3 mL ethyl acetate in a small vial, then surrounding the vial with hexanes inside of a larger vial. After several days of allowing the vapors to diffuse, crystals suitable for X-ray diffraction grew on the inside wall of the small vial.

Crystals of phase **2** were also grown by dissolving 10.5 mg of the product from milling (1:2.5 ratio RSV:4AP) in 2 mL ethyl acetate in a small vial, then vapor diffusing against hexanes. After several days of vapor diffusion, crystals suitable for X-ray diffraction grew on the inside wall of the vial.

2. Single Crystal X-ray Diffraction (SCXRD) Data

Data were collected on a Rigaku XtaLAB Synergy-i Kappa diffractometer equipped with a PhotonJet-i X-ray source operated at 50 W (50kV, 1 mA) to generate Cu Kα radiation (λ = 1.54178 Å) and a HyPix-6000HE HPC detector. Crystals were transferred from the vial to a glass slide in type NVH immersion oil by Cargille. A Leica optical microscope was used to identify a suitable specimen for X-ray diffraction from a representative sample of the material. The crystal and a small amount of oil were collected on a MiTeGen cryoloop and transferred to the instrument where it was placed under a cold nitrogen stream (Oxford) at 100 K, where it was maintained at 100 K throughout the duration of the experiment. The sample was optically centered with the aid of a video camera to ensure that no translations were observed as the crystal was rotated through all positions. The crystal was measured for size, morphology, and color.

After data collection, the unit cell was re-determined using a subset of the full data collection. Intensity data were corrected for Lorentz, polarization, and background effects using CrysAlisPro.[1] A numerical absorption correction was applied based on a Gaussian integration over a multifaceted crystal and followed by a semi-empirical correction for absorption applied using the program SCALE3 ABSPACK.[2] The program SHELXT[3] was used for the initial structure solution and SHELXL[4] was used for the refinement of the structures. Both of these programs were utilized within the OLEX2[5] software. Hydrogen atoms bound to carbon, oxygen, and nitrogen atoms were located in the difference Fourier map and were geometrically constrained using the appropriate AFIX commands, except where otherwise noted.

Refinement details:

RSV-4AP phase **1**: Proton transfer was observed between N1 and N3 of the 4-AP molecules. Both hydrogen atoms (H1A and H3B) could be located in the difference Fourier map and were split into parts A and B and allowed to freely refine to a stable occupancy. H1A refined to 0.720 and H3B refined to 0.280. A G-level alert is present in the checkCIF as a result of successfully modeling the non-integer atoms.

Table S1. X-ray data for phase **1** and phase **2**.

	phase 1	**phase 2**
Compound formula	$C_{38}H_{36.12}N_4O_6$	$C_{24}H_{26}N_4O_4$
Formula mass	644.71	434.49
Crystal system	triclinic	monoclinic
Space group	*P*-1	$P2_1$
a/Å	10.2376(5)	10.1320(2)
b/Å	12.0637(5)	7.84810(10)
c/Å	14.1752(6)	14.9008(3)
α/°	77.506(4)	90
β/°	70.733(4)	108.952(2)
γ/°	85.063(4)	90
V/Å^3	1613.29(13)	1120.64(4)
ρ_{calc} / g·cm^{-3}	1.327	1.288
T/K	100.00(10)	100.01(10)
Z	2	2
Radiation Type	Cu Kα	Cu Kα
Wavelength, Å	1.54184	1.54184
Absorption coefficient, μ/mm^{-1}	0.738	0.729
F(000)	680.0	460.0
Crystal Size (mm^3)	0.1 × 0.08 × 0.05	0.09 × 0.07 × 0.04
Reflections collected	40587	16782
No. of independent reflections	6739	3946
No. of reflection (I > 2σ(I))	5581	3608
Data/restraints/parameters	6739/0/451	3946/1/300
R_{int}	0.0484	0.0513
R1 (I > 2σ(I))	0.0406	0.0334
wR(F^2) (I > 2σ(I))	0.1008	0.0815
R1 (all data)	0.0506	0.0375
wR(F^2) (all data)	0.1060	0.0836
Goodness-of-fit on F^2	1.047	1.049
CCDC deposition number	2473745	2473744

3. Powder X-ray Diffraction (PXRD) Patterns

PXRD patterns were collected using a Rigaku Miniflex 6G benchtop powder diffractometer in Bragg-Brentano geometry. An X-ray diffraction pattern was obtained by scanning a 2θ range of 3-60°, step size = 0.02°, and scan time of 5°/minute. The X-ray source was Cu Kα radiation (λ =1.5418 Å) with an anode voltage of 40 kV and a current of 15 mA. Diffraction intensities were recorded on a position sensitive detector (D/teX Ultra).

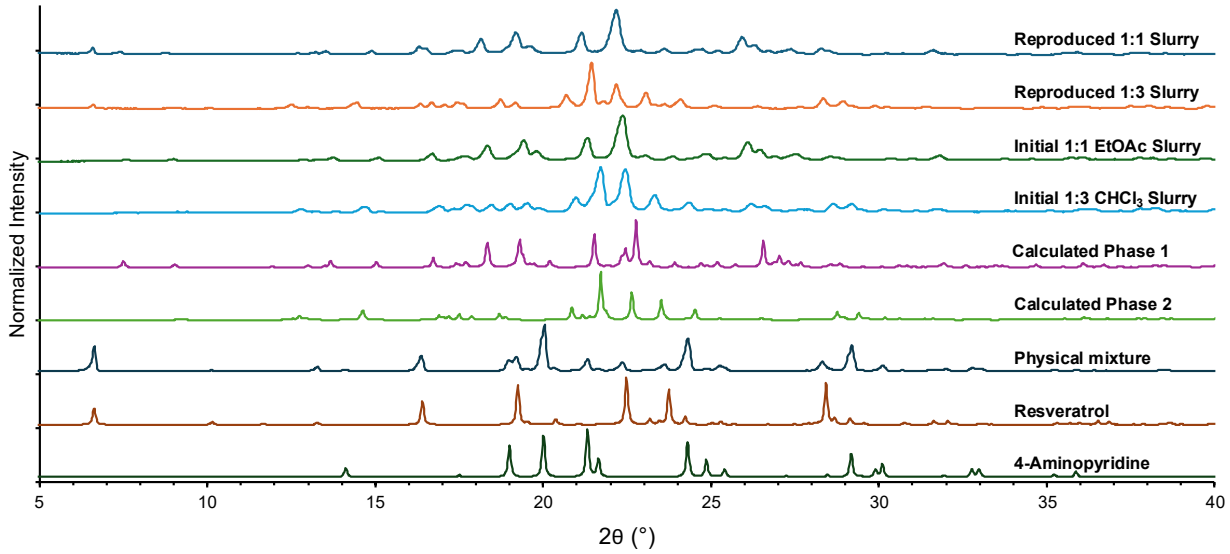

Figure S1. PXRD patterns of phase **1** and phase **2** obtained from initial slurry experiments. Individual components and a physical mixture are shown for comparison.

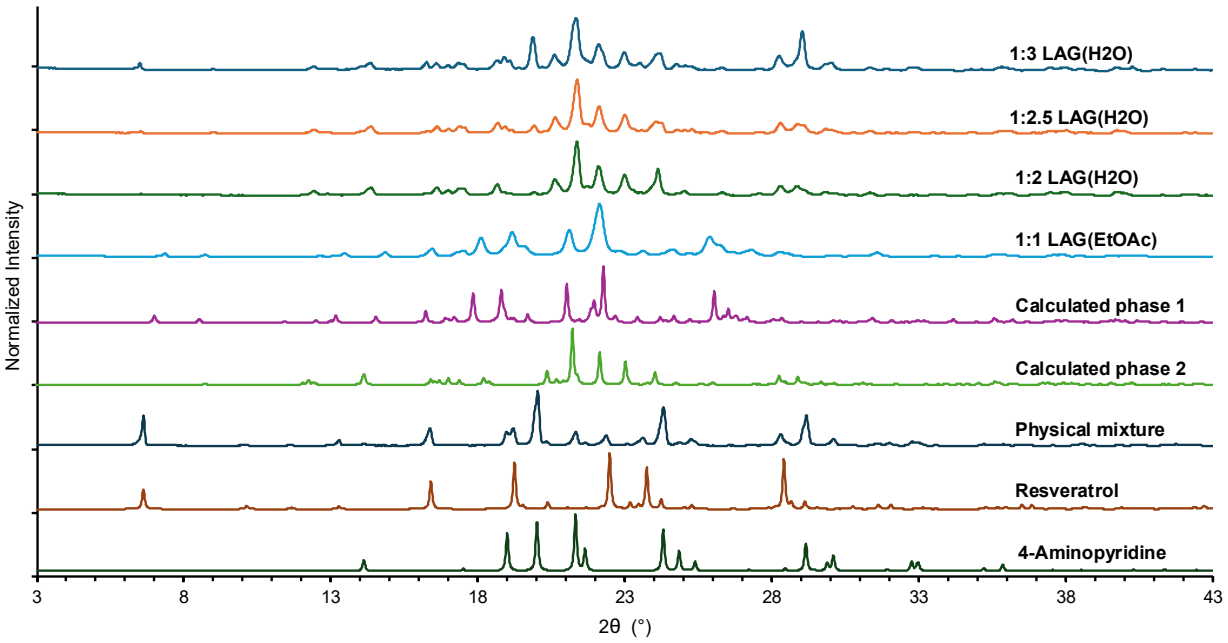

Figure S2. PXRD patterns of powders obtained from LAG experiments. Calculated patterns from SCXRD data are shown. The calculated phase **1** and phase **2** patterns were shifted by -0.5° 2θ to account for difference in collection temperature.

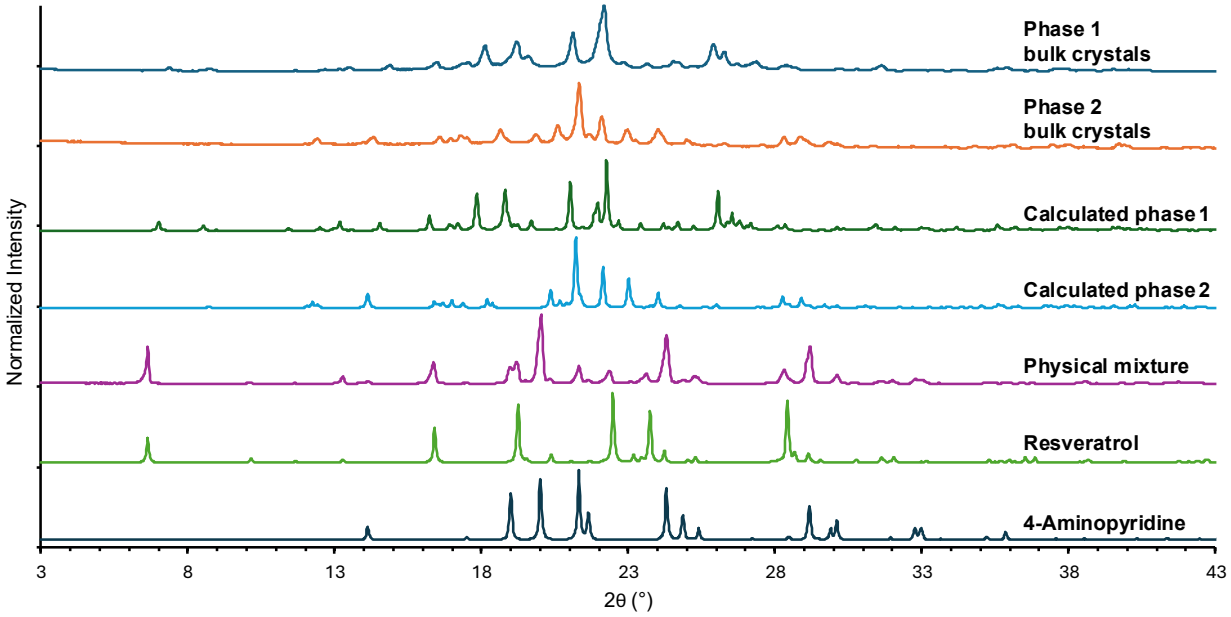

Figure S3. PXRD patterns of bulk crystals produced from solution crystallization. Calculated patterns from SCXRD data are shown. The calculated patterns for phase **1** and phase **2** were shifted by -0.5° 2θ to account for difference in data collection temperature.

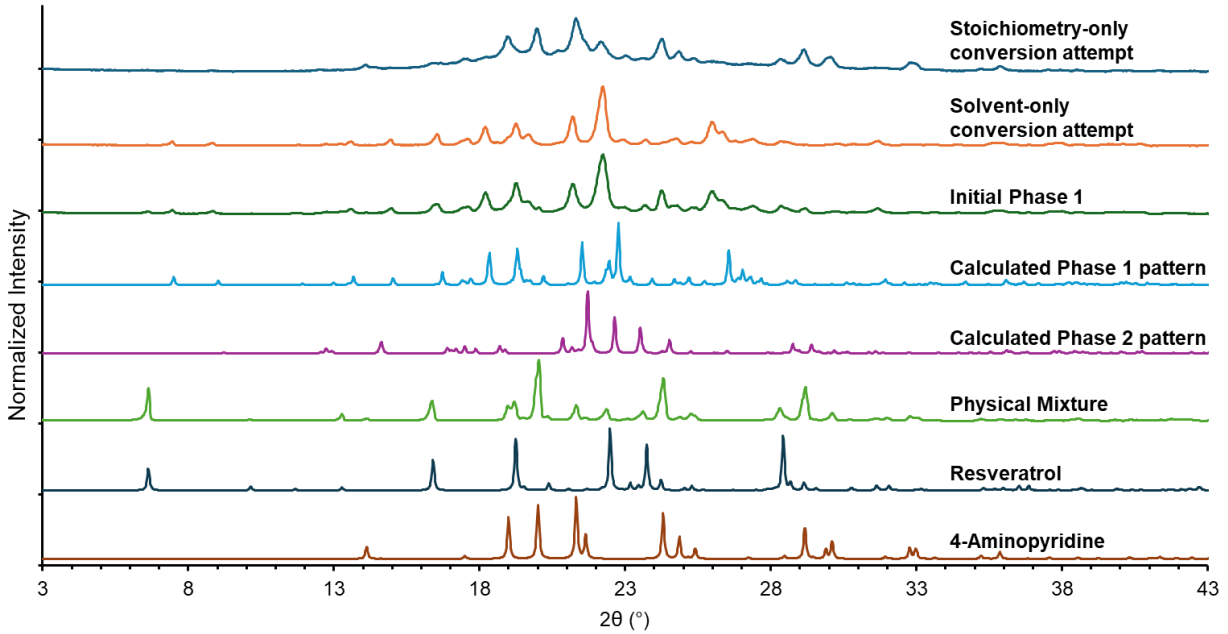

Figure S4. PXRD patterns of different conditions for attempted conversion (stoichiometry only, solvent only) of phase **1** into phase **2**.

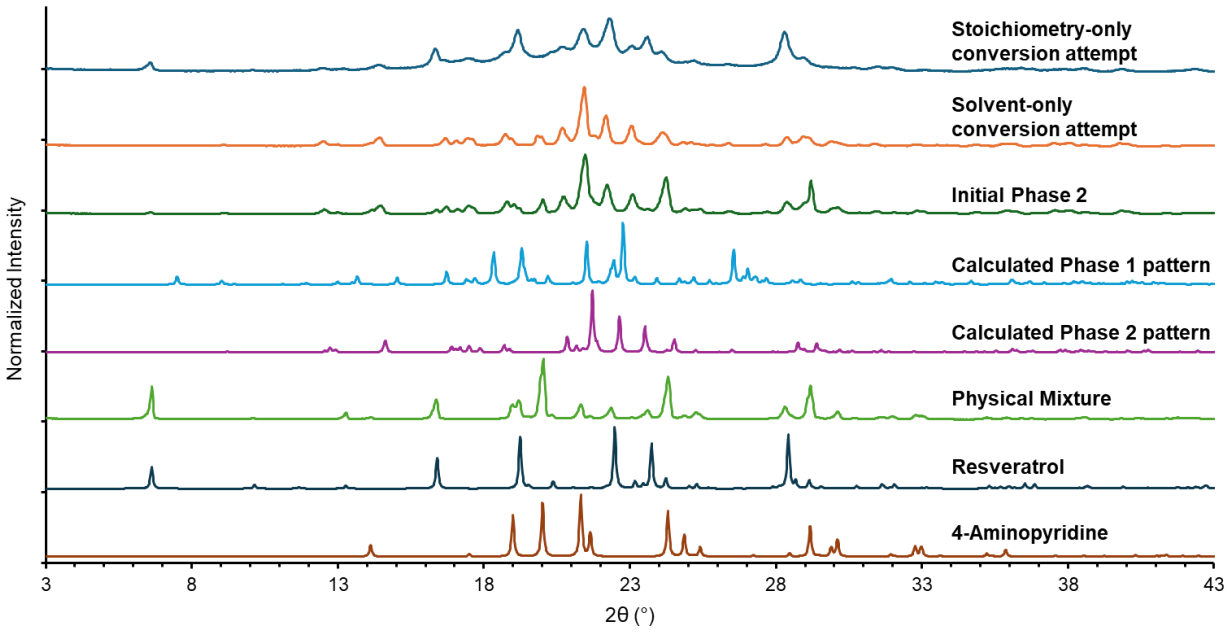

Figure S5. PXRD patterns of different conditions for attempted conversion (stoichiometry only, solvent only) of phase **2** into phase **1**.

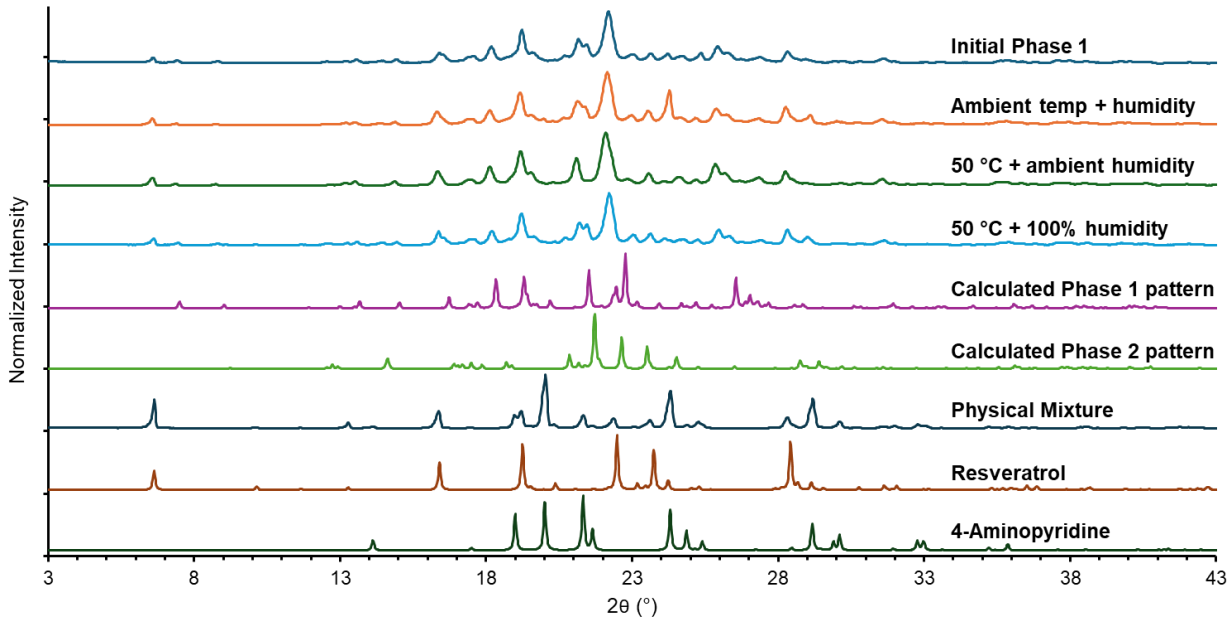

Figure S6. PXRD patterns for benchtop stability testing of phase **1** over a period of 1 week. Ambient temperature throughout testing duration was ca. 20 °C, and ambient humidity was ca. 30%.

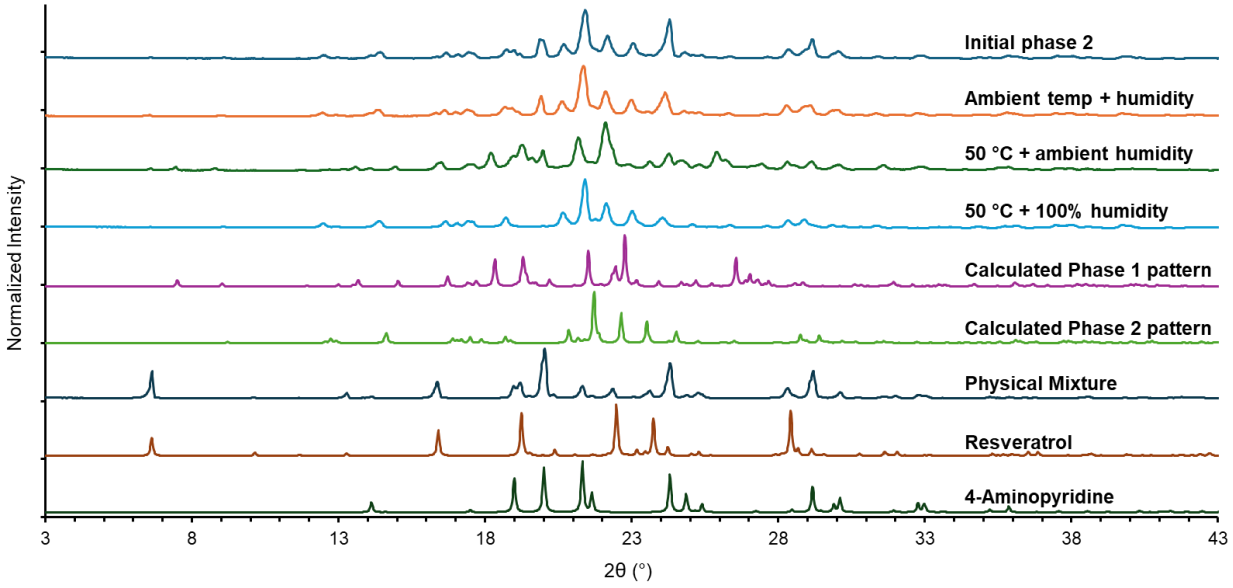

Figure S7. PXRD patterns for benchtop stability testing of phase **2** over a period of 1 week. Ambient temperature throughout testing duration was ca. 20 °C, and ambient humidity was ca. 30%.

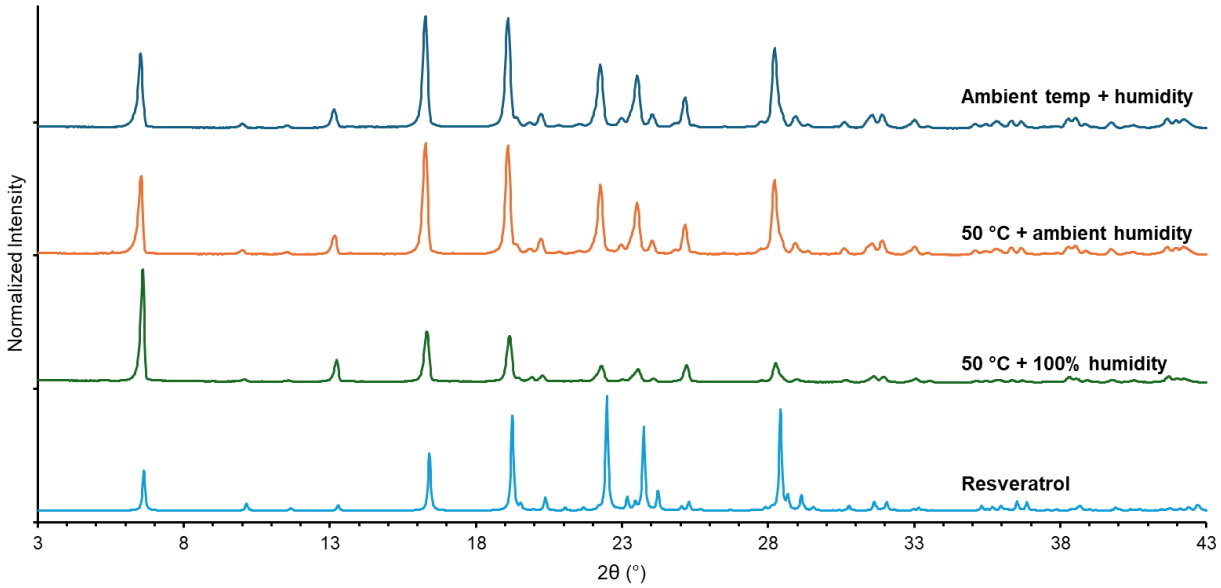

Figure S8. PXRD patterns for benchtop stability testing of RSV over a period of 1 week. Ambient temperature throughout testing duration was ca. 20 °C, and ambient humidity was ca. 30%.

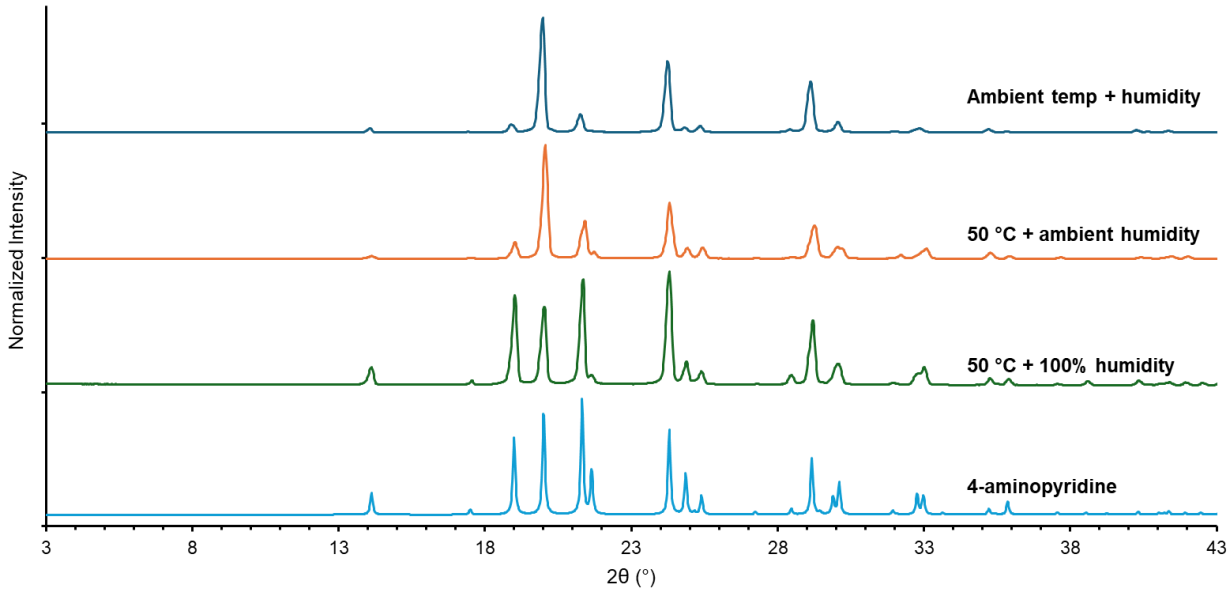

Figure S9. PXRD patterns for benchtop stability testing of 4AP over a period of 1 week. Ambient temperature throughout testing duration was ca. 20 °C, and ambient humidity was ca. 30%.

4. Fourier Transform Infrared (FTIR) Spectroscopy Data

FTIR data were collected using an Agilent Carey 630 FTIR Spectrometer equipped with an ATR sampling module.

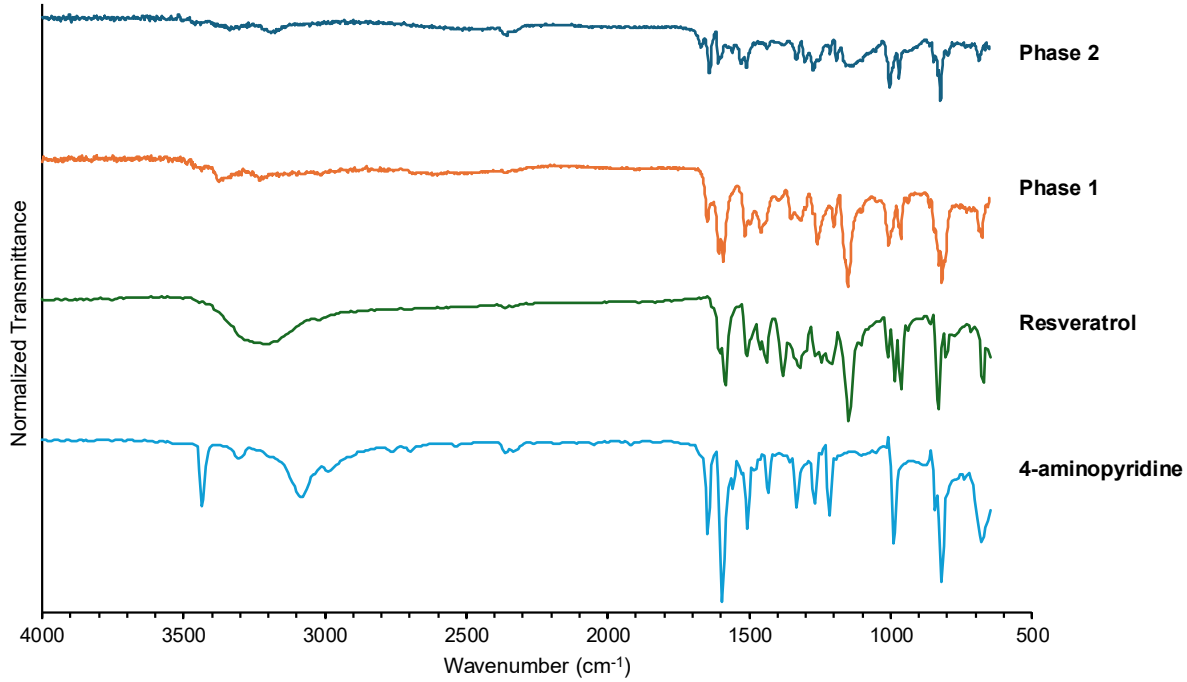

Figure S10. FTIR spectra of phase **1**, phase **2**, RSV, and 4AP.

Table S2. Notable signals from the FTIR spectra of the individual components and ionic cocrystals.

Sample	O-H stretch (cm^{-1})	N-H stretch (cm^{-1})	C=N stretch (cm^{-1})	Aromatic stretch (cm^{-1})	C-O stretch (cm^{-1})
4AP	-	3429 3302	1647	1595 1505	-
RSV	3205	-	-	1610 1580 1505	1148
Phase **1**	broad	3382 3222	1651	1604 1593 1517 1489	1149
Phase **2**	broad	3332 3199	1638	1606 1595 1524 1511	1187

5. Nuclear Magnetic Resonance (NMR) Spectroscopy Data

^{1}H NMR data were collected using a Bruker AVII+ 300 MHz spectrometer. Single crystals of either salt were dissolved in DMSO-d_6 for data collection.

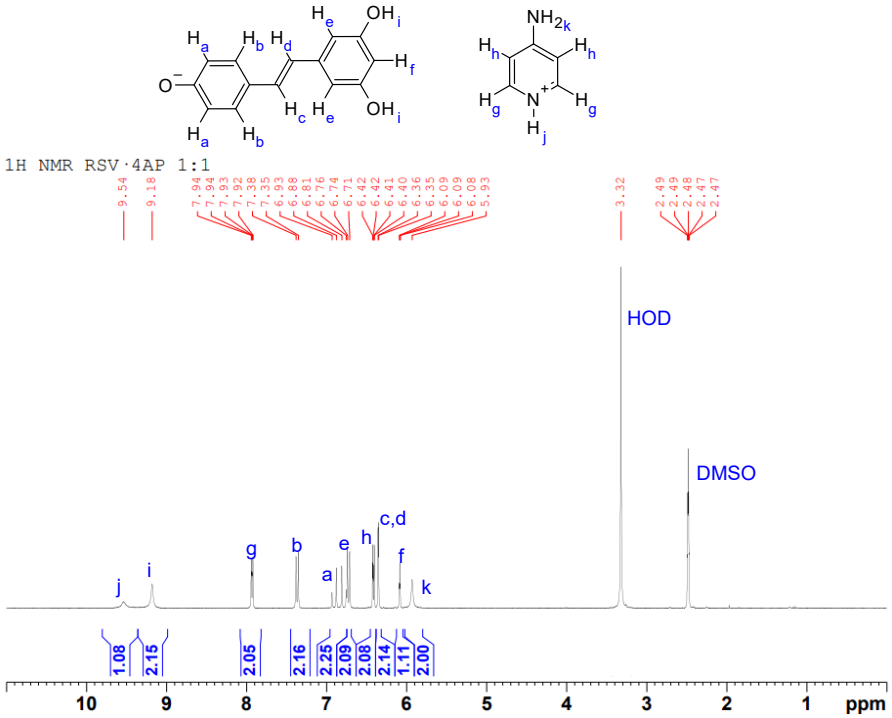

Figure S11. ^{1}H NMR spectrum of phase **1**.

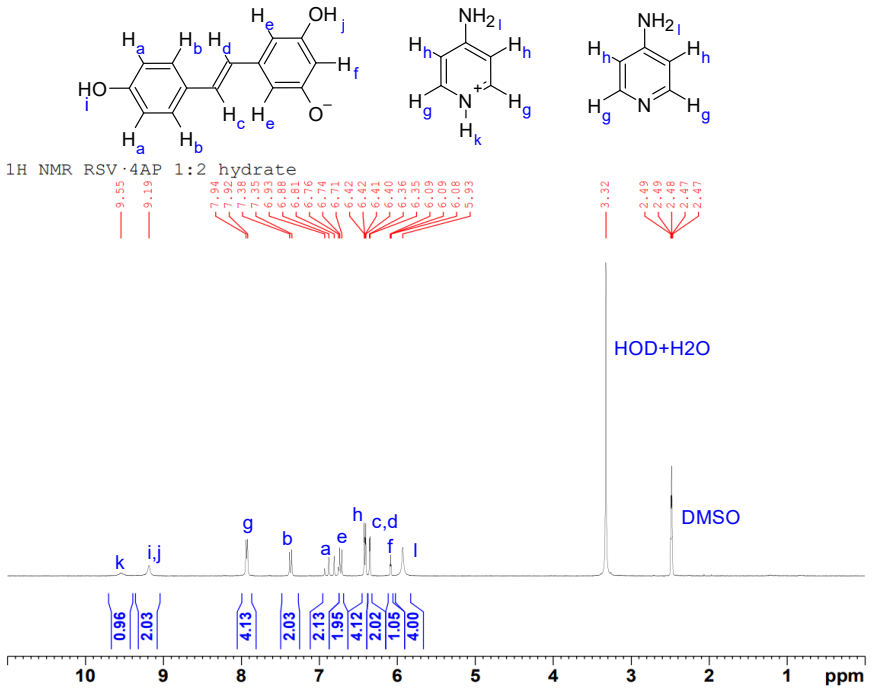

Figure S12. ^{1}H NMR spectrum of phase **2**.

6. Additional Crystal Structure Images

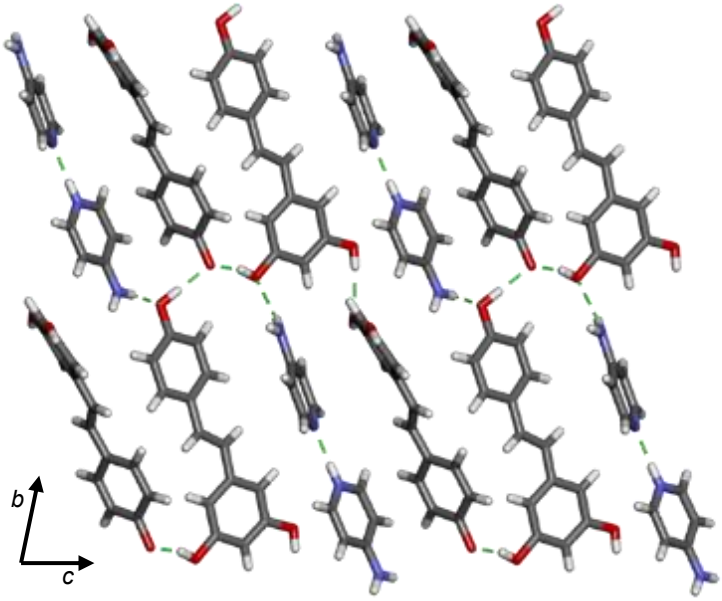

Figure S13. X-ray crystal structure of phase **1** depicting hydrogen bonding along the *bc* plane. The minor disordered site has been omitted for clarity.

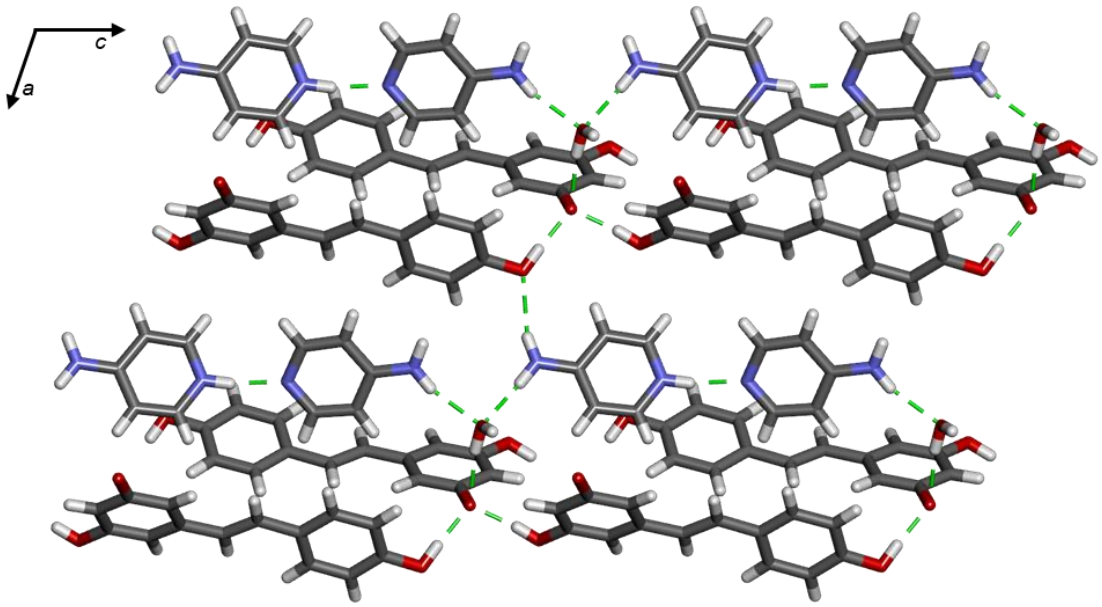

Figure S14. X-ray crystal structure of phase **2** depicting hydrogen bonding along the *ac* plane.

7. Differential Scanning Calorimetry (DSC) Data

DSC data was collected using a TA Instruments DSC250. An RCS 90 refrigerated cooling system was equipped, using a nitrogen atmosphere (50 mL/min). Samples were run in aluminum pans with hermetic lids, at a heating rate of 10 °C/min.

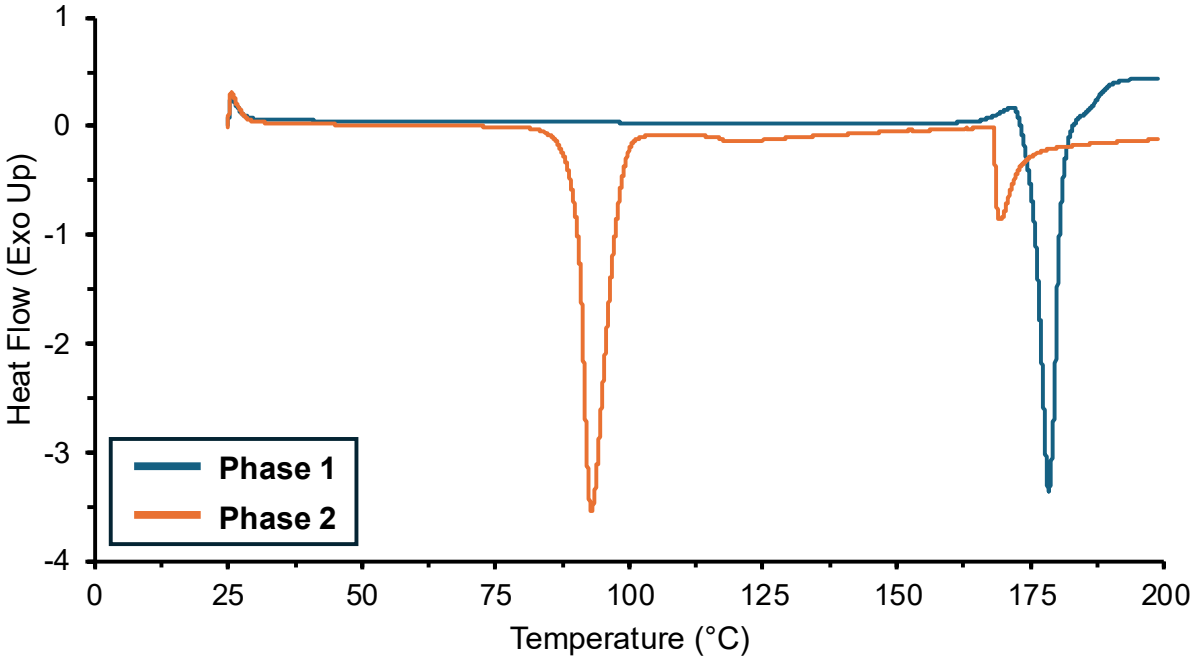

Figure S15. DSC data for phase **1** and phase **2**. Melting point of phase **1** is observed at ca. 178 °C. Loss of water from phase **2** is observed ca. 93 °C, and melting point ca. 169 °C.

8. Thermogravimetric Analysis (TGA) Data

TGA data was collected using a TA Instruments TGA Q50. Samples were run in a platinum pan, with a heating rate of 10°C/min. A nitrogen atmosphere was used with gas flow set at 40 mL/min.

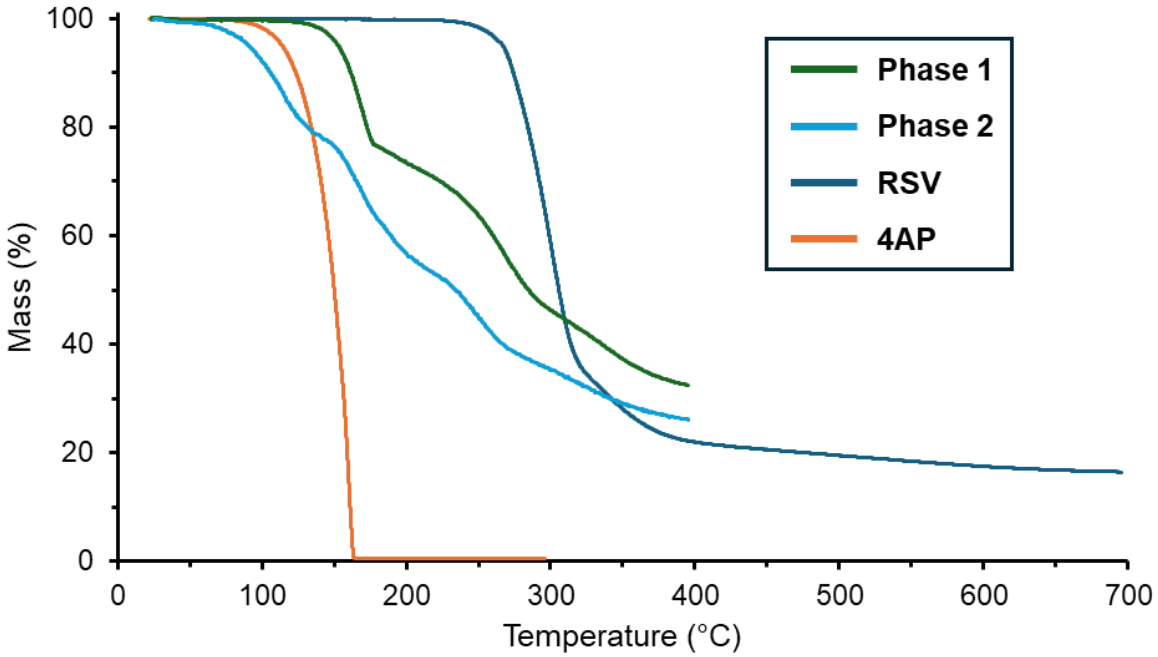

Figure S16. TGA thermograms of RSV, 4AP, phase **1**, and phase **2**. Onsets are noted in the table below.

Table S3. Onset temperatures for thermal events in the TGA thermograms.

Sample	Water loss (˚C)	First onset (˚C)	Second onset (˚C)
Phase 1	-	153	245
Phase 2	89	155	235
RSV	-	274	
4AP	-	143	

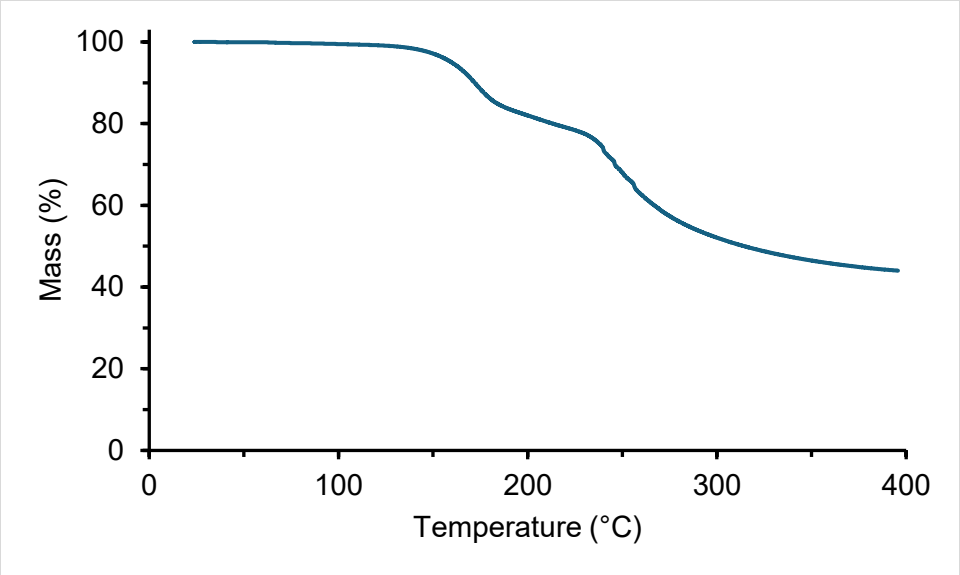

Figure S17. TGA thermogram of product obtained from conversion of phase **2** to phase **1**. First onset at ca. 156 ˚C, and second onset observed at ca. 235 ˚C. No loss of water was observed.

9. Solubility Data

Solubility testing of both phases was performed in pH 1.2 buffer, in triplicate. Buffer was prepared by adding 1.00 g NaCl and 3.5 mL of 12.1 M HCl to a 500 mL volumetric flask, then diluting to the mark with distilled water. A stock solution was prepared by dissolving approximately 10 mg of either phase in 250 mL buffer, then let sit for one hour before preparing standard solutions. Standard solutions were prepared by diluting varying amounts of stock solution to 10 mL with buffer.

Table S4. Solubility of both phases in pH 1.2 buffer

	Concentration (mg/mL)	λ_{max}
Phase **1**	3.71 ± 0.05	209 nm
Phase **2**	6.70 ± 0.95	208 nm

10. Electrostatic Potential Maps

Electrostatic potential maps were generated in Spartan'24,[6] version 1.3.1. Calculations were performed using DFT method, using the B3LYP basis set and 6-311++G** level of theory. Unless otherwise stated, all calculations used molecules modeled in their crystalline geometry without additional geometry optimization.

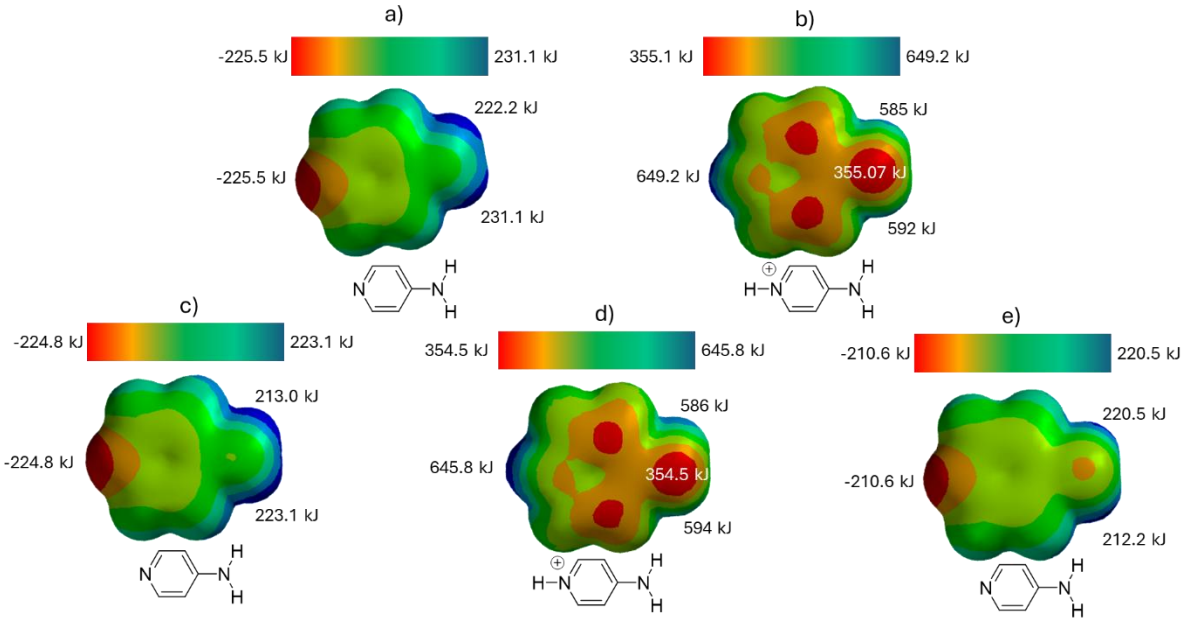

Figure S18. Electrostatic potential maps for a) the primary neutral 4AP molecule in phase **1**, b) the primary cation $4AP^+$ molecule in phase **1**, c) the neutral 4AP molecule in phase **2**, d) the $4AP^+$ cation in phase **2**, and e) a 4AP molecule that was subjected to geometry optimization for reference. The skeletal structure below each molecule is shown for clarity. Note the numerical scales on parts a, c, and e are different than parts b and d.

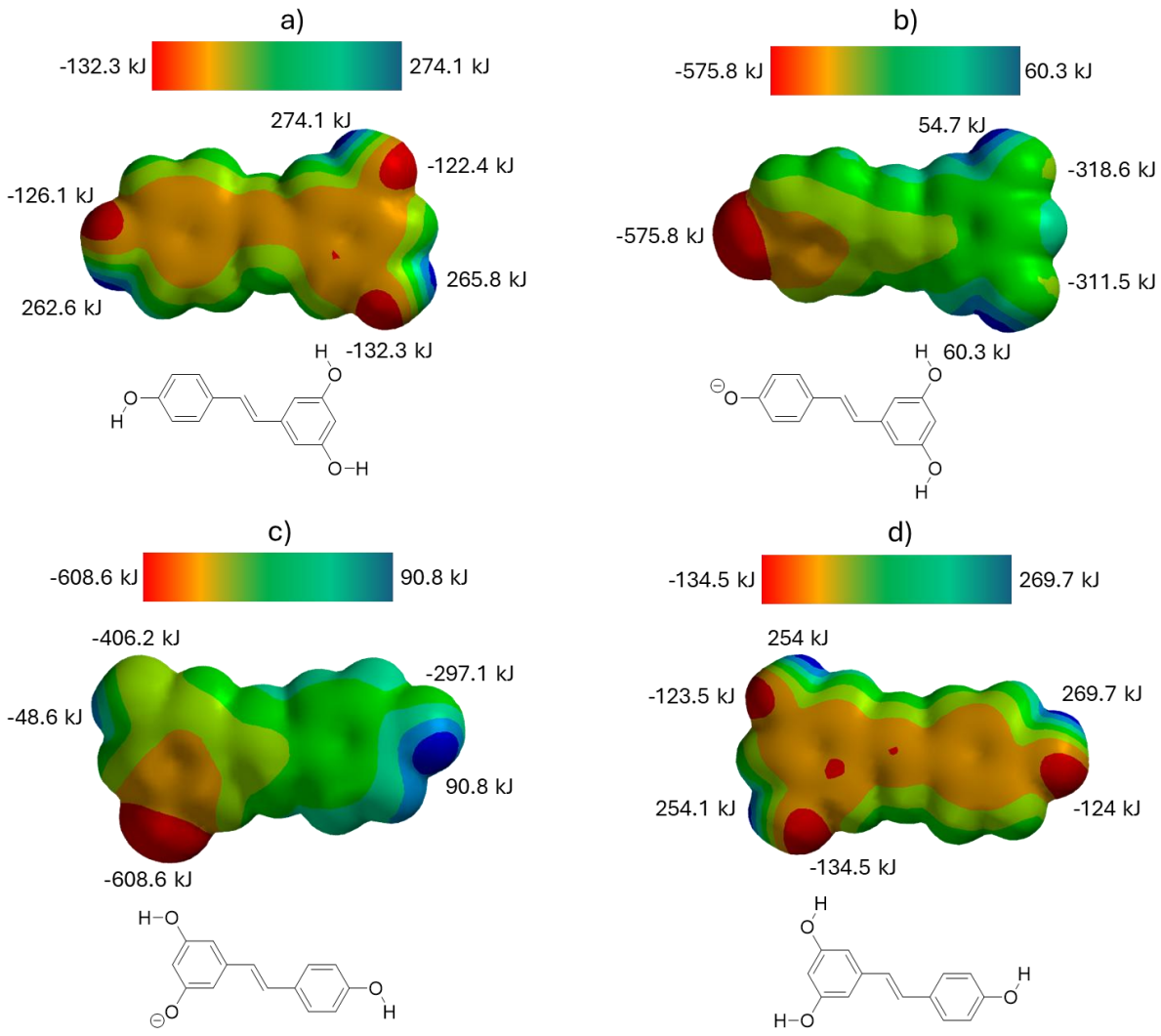

Figure S19. Electrostatic potential maps for a) neutral RSV in phase **1**, b) the RSV^- anion in phase **1**, c) the RSV^- in phase **2**, and d) a RSV molecule that was subjected to geometry optimization for reference. The skeletal structure below each molecule shows the conformation of the hydroxy groups in the structure.

11. Energy Calculations

Lattice energies and interaction energies were calculated using the VisualHabit[7] implementation in Mercury v. 2025.3.3.[8] The DREIDING II forcefield[9-11] was used, with Evjen electrostatic correction[12] and a limiting radius of 30 Å.

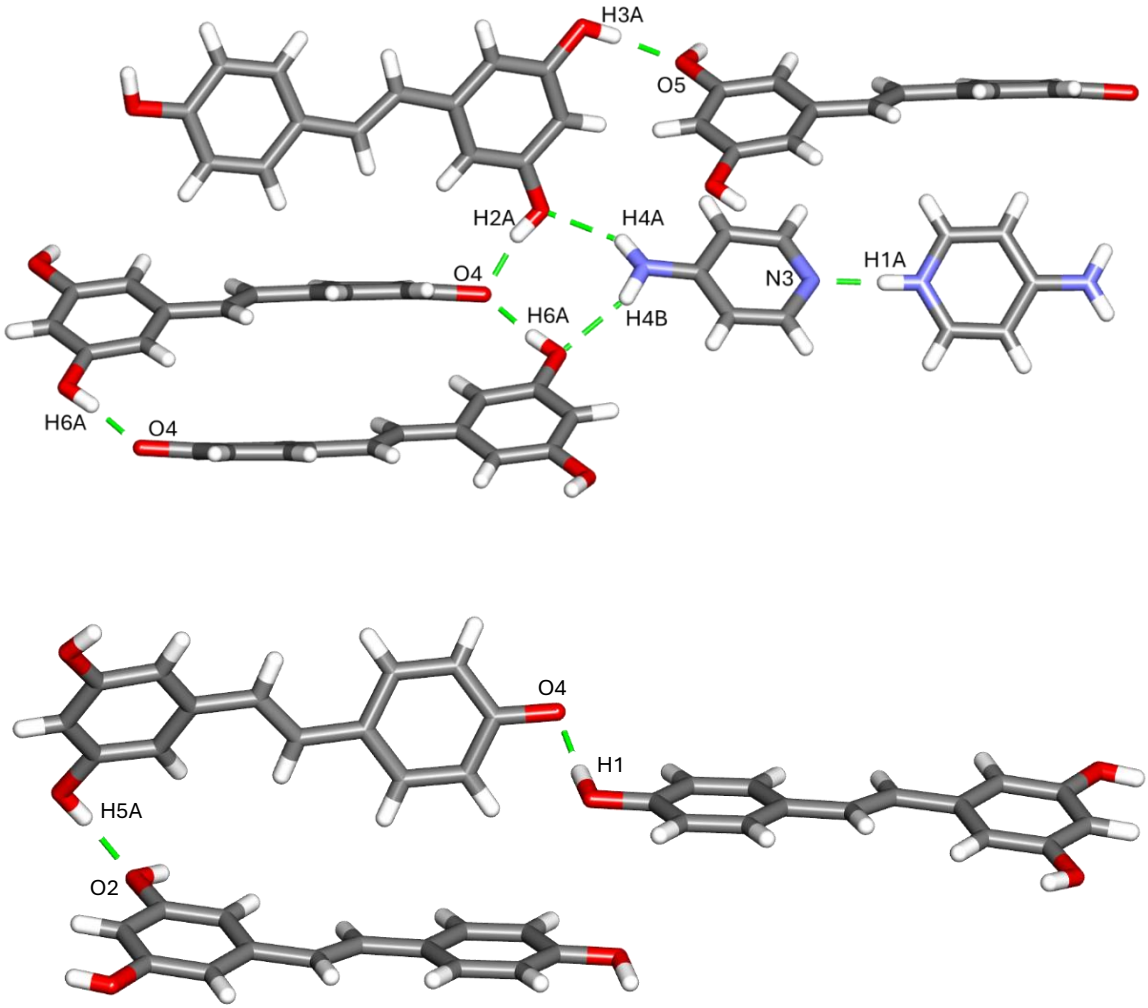

Figure S20. Crystal structure images of phase **1** highlighting relevant atoms for intermolecular interaction energy calculations.

Table S5. Interaction energies for intermolecular interactions in phase **1** (see figure above for numbering).

H Bond Pair	D(H) ⋯ A (Å)	H ⋯ A (Å)	Electrostatic Energy (kJ/mol)	van der Waals Energy (kJ/mol)	Hydrogen Bond Energy (kJ/mol)	Interaction Energy (kJ/mol)
O6, H6A ⋯ O4	2.694	1.858	21.495	11.764	-27.606	5.653
N1, H1A ⋯ N3*	2.691	1.811	-21.781	13.304	-14.137	-22.613

O3, H3A ··· O5	2.834	1.997	-5.196	2.004	-13.761	-16.953
O5, H5A ··· O2	2.677	1.847	-3.356	-2.064	-12.955	-18.376
O1, H1 ··· O4	2.665	1.750	-24.704	12.615	-11.808	-23.897
N2, H2B ··· O1	3.026	2.151	-6.342	-0.785	-10.222	-17.350
N4, H4A ··· O2	3.048	2.202	-1.049	-1.106	-6.128	-8.283
N4, H4B ··· O6	3.005	2.166	-1.936	-0.672	-5.847	-8.454
O2, H2A ··· O4	2.492	1.671	-28.813	19.759	3.057	-5.998

* For disordered groups, only the major occupancy was used.

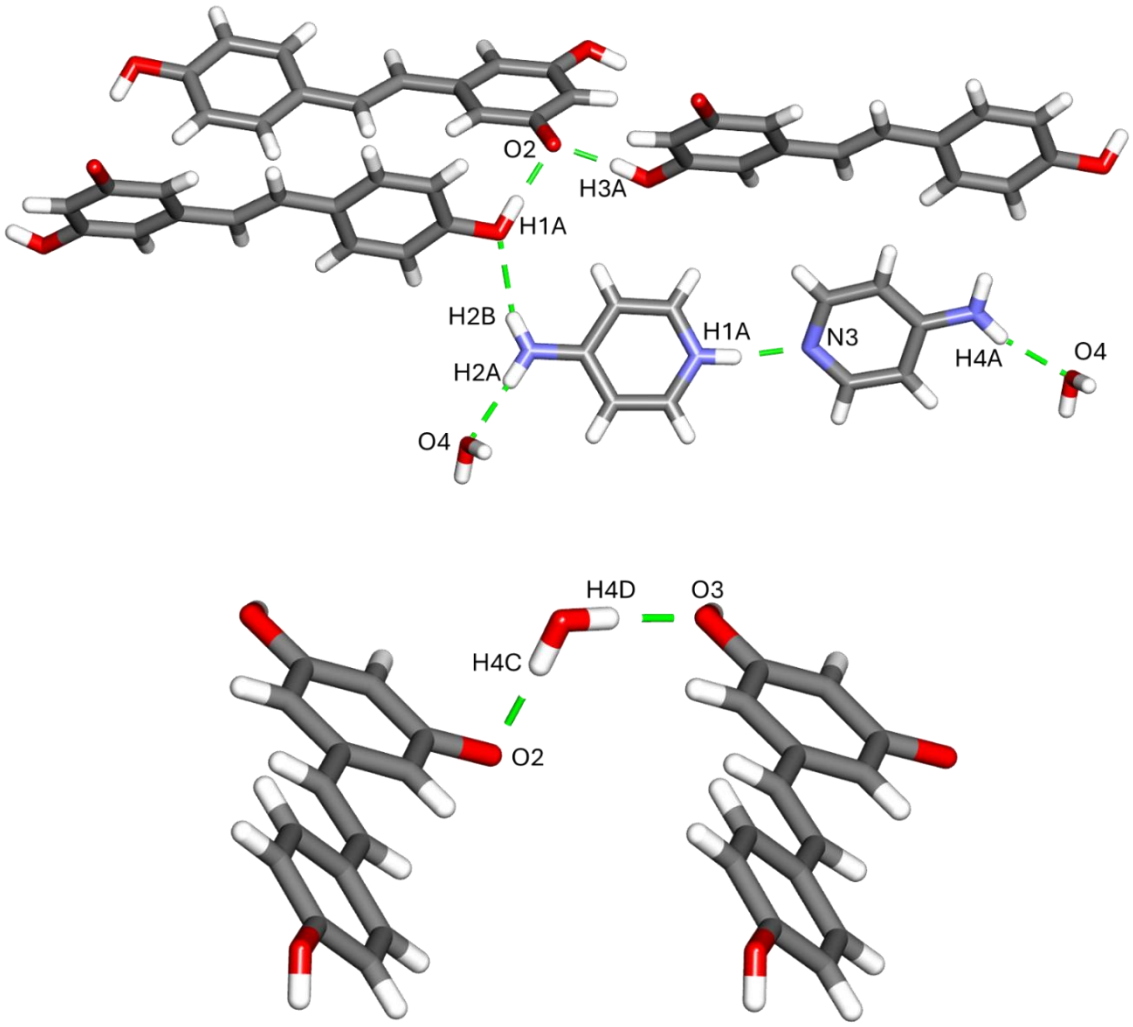

Figure S21. Crystal structure images of phase **2** highlighting relevant atoms for intermolecular interaction energy calculations.

Table S6. Interaction energies for intermolecular interactions in phase **2** (see figure above for numbering).

H Bond Pair	D(H) ⋯ A (Å)	H ⋯ A (Å)	Electrostatic Energy (kJ/mol)	van der Waals Energy (kJ/mol)	Hydrogen Bond Energy (kJ/mol)	Interaction Energy (kJ/mol)
O4, H4D ⋯ O3	2.732	1.834	-9.640	7.842	-14.399	-16.197
N1, H1A ⋯ N3	2.766	1.896	-20.356	6.791	-13.606	-27.171
O4, H4C ⋯ O2	2.850	1.974	-20.715	3.336	-13.165	-30.544
N4, H4A ⋯ O4	2.960	2.098	-0.958	1.218	-10.508	-10.248
N2, H2A ⋯ O4	2.919	2.070	-2.565	1.527	-10.329	-11.367
O1, H1 ⋯ O2	2.563	1.731	36.911	8.092	-6.796	38.206
N2, H2B ⋯ O1	3.007	2.198	-52.034	-0.855	-6.751	-59.640
O3, H3A ⋯ O2	2.516	1.682	103.892	23.742	-0.889	126.745

Table S7. Lattice energies for phase **1** and phase **2**.

Ionic cocrystal	Total Electrostatic Energy (kJ/mol)	Total van der Waals Energy (kJ/mol)	Total Hydrogen Bond Energy (kJ/mol)	Total Lattice Energy (kJ/mol)
Phase **1**	-132.330	-30.438	-44.193	-206.961
Phase **2**	-118.173	-10.648	-39.265	-168.085

12. References

1. CrysAlis^{Pro} (2018) Oxford Diffraction Ltd.

2. SCALE3 ABSPACK (2005) Oxford Diffraction Ltd.

3. G. M. Sheldrick, SHELXT - Integrated space-group and crystal-structure determination, *Acta Crystallogr., Sect. A: Found. Adv.,* 2015, **A71**, 3-8.

4. G. M. Sheldrick, Crystal structure refinement with SHELXL, *Acta Crystallogr., Sect. C: Struct. Chem*., 2015, **C71**, 3-8.

5. O. V. Dolomanov, L. J. Bourhis, R. J. Gildea, J. A. K. Howard and H. Puschmann, OLEX2: a complete structure solution, refinement and analysis program, *J. Appl. Cryst*., 2009, **42**, 339-341.

6. Spartan'24 v1.3.1. 2025, Wavefunction, Inc., Irvine, CA. https://www.wavefun.com/spartan

7. G. Clydesdale, R. Docherty, and K. J. Roberts. *Comput. Phys. Commun.*, 1991, **64**, 311–328.

8. C. F. Macrae, I. Sovago, S. J. Cottrell, P. T. A. Galek, P. McCabe, E. Pidcock, M. Platings, G. P. Shields, J. S. Stevens, M. Towler and P. A. Wood. *J. Appl. Cryst.*, 2020, **53**, 226-235.

9. S.L. Mayo, B.D. Olafson and W.A. Goddard III. *J. Phys. Chem.*, 1990, **94**, 8897. (Table II)

10. D.E. Williams. *J. Chem. Phys.*,1966, **45**, 3770.

11. N.L. Allan, A.L. Rohl, D.H. Gay, R.A. Catlow, R.J. Davey and W.C. Mackrodt. *J. Chem. Soc. Faraday Discuss.*, 1993, **95**, 273.

12. H. M. Evjen. *Phys. Rev*., 1932, **39**, 675.